Research Article

Nano Biomed Eng

Silicon-based Tubular Micromotor with SERS Traceability and Magnetic–Thermal Dual Responsiveness

Sijie Zhang, Gaoqiang Yin, Zuyao Wang, Lei Wu, Kuo Yang, Ruohu Zhang, Shenfei Zong ✉, Zhuyuan Wang ✉, Yiping Cui

Advanced Photonics Center, School of Electronic Science and Engineering, Southeast University, Nanjing 211189, China

✉ Corresponding authors. E-mails: Shenfei Zong, sfzong@seu.edu.cn; Zhuyuan Wang, wangzy@seu.edu.cn

Received: Nov. 8, 2024; **Revised:** Jan. 24, 2025; **Accepted:** Feb. 6, 2025

Citation: S.J. Zhang, G.Q. Yin, Z.Y. Wang, et al. Silicon-based tubular micromotor with SERS traceability and magnetic–thermal dual responsiveness. *Nano Biomedicine and Engineering*, 2025, 17(2): 263−276.

http://doi.org/10.26599/NBE.2025.9290118

Abstract

The synergistic strategy based on magnetic hyperthermia and free radical therapy demonstrates tremendous potential in inducing effective tumor cell death. Therefore, the development of a novel multifunctional micromotor with magnetic-thermal dual responsiveness is of paramount importance. Here, a novel silicon-based tubular micromotor (SiMMs) is presented, which is fabricated via template-assisted atomic layer deposition (ALD). The SiMMs is specially designed to load 2,2'-azobis(2-midinopropane) dihydrochloride (AAPH), which is an anticancer drug. Firstly, the micromotors were prepared using a polycarbonate (PC) film as a template to grow silicon microtubes via ALD. Then, a multi-step functionalization process was carried out, the silicon microtubes were modified with Fe_3O_4 magnetic nanoparticles and gold core–silver shell nanoparticles to enable magnetic controllability and surface-enhanced Raman scattering (SERS) traceability. Subsequently, aptamers and AAPH were further modified onto the microtubes through a coupling method. Finally, characterizations of SiMMs were conducted, including motion behaviors, fluorescence and SERS signals. Magnetic–hyperthermia synergistic therapy of cancer cells using SiMMs were also investigated. Results indicated that SiMMs exhibit excellent magnetic controllability, targeted drug delivery efficiency, real-time monitoring capabilities, and outstanding cytotoxicity towards cancer cells under an alternating magnetic field (AMF). The novel SiMMs-based drug carrier and synergistic treatment strategy provide a new platform for cancer therapy.

Keywords: micromotor; magnetic field control; surface-enhanced Raman scattering (SERS) tracking; carbon-centered radical; synergistic therapy

Introduction

Cancer stands as a major global public health challenge, posing a serious threat to human well-being [1]. Aside from surgery, radiation therapy and chemotherapy serve as the primary clinical options for cancer treatment. However, these traditional treatment methods carry significant side effects and constraints, including radiation-induced damage to adjacent healthy tissues, chemotherapy-related harm to healthy cells, and potential long-term effects on the immune and nervous systems [2–6]. Consequently, the quest for more stable, effective, and safer cancer treatment approaches remains a key focus in the

medical domain.

In recent years, the development of synergistic treatment strategies combining magnetic hyperthermia and free radicals has advanced rapidly. This approach has shown some success in the treatment of challenging tumors [7]. Magnetic hyperthermia, due to the infinite penetration depth of applied magnetic fields in biological tissues, exhibits tremendous potential in the treatment of deep-seated tumors [8–11]. Unlike phototherapy and other methods relying on light penetration, magnetic hyperthermia is not limited by tissue absorption and scattering, allowing direct action on deep tissues within the body [12]. The principle behind magnetic hyperthermia involves implanting magnetic nanoparticles within biological tissues and applying an external alternating magnetic field (AMF). These magnetic particles generate heat under the influence of AMF, raising the temperature of the tumor tissue to achieve a therapeutic effect [13–15]. However, the magnetic heating efficiency of magnetic nanoparticles is low, thus magnetic hyperthermia therapy is typically utilized as a supplementary treatment to enhance tumor sensitivity to radiation therapy or chemotherapy [16–18]. Free radicals are highly reactive species that can interact with lipids, proteins, and DNA within cells, resulting in cellular dysfunction and death [19, 20]. This additional cellular toxicity mechanism can enhance the effectiveness of magnetic hyperthermia therapy [21]. Therefore, the combination of magnetic hyperthermia with free radical treatment strategies can enhance therapeutic effectiveness, increase tumor-killing capacity, and reduce damage to normal tissues. This approach offers a new and effective means for cancer treatment [11, 15, 22].

Based on the treatment strategy mentioned above, a variety of different nanoparticles have been studied for cancer therapy, including gold nanoparticles and magnetic iron oxide nanoparticles (MIONs) [23–26]. MIONs are among the most attractive particles for clinical applications, which are typically composed of a magnetic iron oxide core stabilized by a biocompatible hydrophilic surface coating [27]. MIONs can be modified to carry drugs and guided to tumor sites using an external magnetic field. Once positioned within the tumor, applying an AMF not only generates hyperthermia but also triggers drug release, leading to the release of free radicals for localized therapy [11]. Combined therapeutic strategies involving MIONs have significant potential in cancer treatment, but large-scale clinical translation faces ongoing challenges. One of the most significant limitations is the difficulty in targeting and locating tumor cells within the tumor, aside from real-time monitoring and tracking [14].

As drug carriers, micro/nanomotors with various morphologies, such as wire motors, Janus motors [28–30], helical motors [31, 32], and tubular motors [33–35], have been extensively studied. Reports suggest that linear-shaped nanoparticles (like tubular and helical) exhibit significant advantages in circulation time in the bloodstream [36]. Additionally, silica nanoparticles have found wide application in drug delivery systems owing to their structured mesoporous architecture, large surface area, outstanding biocompatibility, and the simplicity of surface modification [37, 38]. Through surface-specific modifications or functionalization, the multifunctional nature enables the integration of multiple functional units [39], addressing the aforementioned issues associated with traditional MIONs and significantly enhancing the overall effectiveness of treatment strategies.

In this case, micro-sized silicon-based microtubes are used as drug carriers for micromotor (SiMMs). Initially, the required silicon microtube carrier is grown using a PC film as a template through atomic layer deposition (ALD). The advantage of this technology lies in its ability to rapidly and economically produce a large number of silicon-based carriers [40]. Subsequently, dichloromethane is employed to dissolve the outer PC film, releasing the silicon microtubes into the solvent, which are then obtained in a purified form through centrifugal separation. A series of modification steps are then carried out on the prepared silicon microtubes. Firstly, the silicon microtubes are labeled with fluorescein isothiocyanate (FITC) to provide fluorescence for subsequent co-localization imaging experiments. Next, magnetic Fe_3O_4 nanoparticles and gold core–silver shell nanoparticles are modified onto the microtubes, imparting them with magnetic controllability and surface-enhanced Raman scattering (SERS) tracking capabilities. Finally, aptamers and AAPH are conjugated onto the tubes, forming the entire SiMMs. These modifications endow the SiMMs with a dual treatment mode

combining magnetic hyperthermia and free radicals, along with essential engineerable functionalities for clinical applications.

The unique advantages of SiMMs over previous micromotors or nanoparticle-based systems lie in their multifunctional integration and enhanced therapeutic potential. Specifically, SiMMs combine magnetic control, free radical generation, and real-time monitoring capabilities into a single platform. This integration allows for precise targeting of tumor cells using an external magnetic field, localized drug delivery, and real-time tracking of the micromotors within biological environments. The dual treatment mode, which merges magnetic hyperthermia with free radical therapy, significantly enhances the cytotoxicity towards cancer cells while minimizing damage to healthy tissues. Moreover, the combination of fluorescence and SERS tracking provides a powerful means for monitoring the treatment process, ensuring high detection accuracy and real-time observation of dynamic changes. These features collectively position SiMMs as a promising candidate for cancer therapy.

Experimental

Materials and instruments

Hexadecyl trimethylammonium bromide (CTAB), tetraethoxysilane (TEOS), and silver nitrate were obtained from Sigma-Aldrich. PC membranes were obtained from Whatman. 3-Aminopropyltriethoxysilane (APTES) and sodium citrate were obtained from Alfa Aesar. Triethanolamine (TEOA) was obtained from Titan. Dichloromethane (CH_2Cl_2), ethanol (EtOH), iron chloride ($FeCl_3$), and ferrous chloride ($FeCl_2$) were all purchased from China National Pharmaceutical Group Corporation. 5,5'-Dithiobis(2-nitrobenzoic acid) (DTNB), 4-mercaptobenzoic acid (4MBA), aqueous ammonia and AAPH were purchased from Aladdin. Chloroauric acid was purchased from Adamas (Shanghai). The NH_2-modified CD63 aptamer(5'-CAC CCC ACC TCG CTC CCG TGA CAC TAA TGC TA-(CH_2)6-NH_2-3) was synthesized by Shanghai Genecore Biotech Co., Ltd. Phosphate-buffered saline (PBS, 10 mmol/L, pH 7.4) was purchased from Beijing Boboson Biotechnology Co., Ltd. H_2DCFDA probe, Calcein/PI cell viability and cytotoxicity assay kit, cell membrane far-red fluorescent probe (DiD) and cell counting kit-8 (CCK-8) were all acquired from Sigma. Breast cancer cells (MDA-MB-231) were obtained from the Cell Bank of Shanghai Institute of Life Sciences, Chinese Academy of Sciences. The culture medium used was 90% Dulbecco's modified Eagle medium (DMEM) (purchased from Nanjing KeyGen Biotech Co., Ltd). The reagents used in the experiment do not require further purification procedures. The water utilized in the experiment is deionized water with a resistivity of 18.25 MΩ·cm.

The sample was characterized and imaged using a scanning electron microscope (SEM, FEI Inspect F50). The morphology and elemental analysis of SiMMs were characterized using a transmission electron microscope (TEM, Tecnai G²T20). The surface potential was analyzed using a particle size analyzer (Zetasizer Nano Series ZS90). SERS spectra were collected using a Raman spectrometer (Horia, model T64000) with a 633-nm He-Ne laser. Fluorescence imaging was performed using a Zeiss Elyra, P.1 microscope equipped with a 100×/1.46 oil immersion objective and an Andor EM-CCD camera (iXon DU897), with image data analyzed using Zeiss ZEN 2012 software. Observations of experimental samples during cell capture experiments were conducted using a laser confocal fluorescence microscope (Olympus, FV1000). AMF (0.8 KW, 20−25 KHz) was generated using an induction magnetic stirrer (IKA, C-MAG HS 7 control).

Synthesis of SiMMs

12.5 mg of CTAB and 10 mg of TEOA were dissolved in 4 mL of deionized water. After complete dissolution, a PC membrane was placed in a 20-mL bottle on a magnetic heating stir plate and heated to 80 °C. Once the temperature stabilized, 5 μL of APTES was added, and the reaction was maintained at a constant temperature of 80 °C for 30 min. Concurrently, a mixture of APTES and TEOS was prepared by combining 15 μL of APTES with 75 μL of TEOS. The concentration of TEOS was adjusted accordingly based on the morphology of the experimental product. After the previous step's 30-min reaction, 30 μL of the mixed solution was added, and the high-temperature reaction continued for 2 h. Upon completion, the heating was discontinued, allowing the temperature of the reaction system to gradually return to ambient conditions under continuous stirring. The PC membrane was

carefully removed using clean forceps and placed in deionized water. Both sides of the membrane were meticulously wiped with a lint-free cotton swab. Stubborn residues were addressed by gently scraping off excess Si-based material using neutral aluminum chloride until the surface became smooth. Subsequently, the membrane was rinsed on both sides with deionized water. To release the SiMMs from the membrane, it was dissolved in CH_2Cl_2. If dissolution was ineffective, ultrasonication was employed. The solution was then centrifuged twice with CH_2Cl_2, EtOH, and deionized water (at 8 000 r/min for 10 min each at –4 °C). Finally, the prepared SiMMs were stored in deionized water.

Synthesis of gold core–silver shell SERS nanoprobes

We added 50 μL of 20% chloroauric acid solution to 100 mL of deionized water, and then heated the reaction system to boiling, followed by adding 4 mL of 1% sodium citrate solution dropwise. We continued heating and stirring the mixture for 30 min until a wine-red color appears. We took 50 mL of the solution and continued stirring (600 r/min). Once the reaction system stabilizes, we added the required Raman molecules (DTNB, 50 μL), and let the reaction proceed for 12 h under stirring conditions.

Surface functionalization and drug loading of SiMMs

1 mg of FITC dye was weighed and mixed with 1.5 mL of deionized water containing SiMMs. The mixture was placed on a shaker overnight for 12 h. Afterward, the solution was centrifuged three times to remove the supernatant, and the fluorescence effect was observed using a fluorescence microscope with a 488-nm laser wavelength.

Next, Fe_3O_4 magnetic nanoparticles were prepared by dissolving 5.4 g of ferric chloride (0.02 mol) and 2 g of ferrous chloride (0.01 mol) in 40 mL of deionized water, heating the solution to 80 °C, rapidly adding 8 mL of ammonia, and stirring vigorously for 1 h. A solution of 3 g of sodium citrate melted in 10 mL of water was then dripped into the above solution and heated to 90 °C for 100 min. After separation using a magnet and washing with water via centrifugation, the magnetic nanoparticles were dissolved in 10 mL of water, resulting in nanoparticles of ~ 50 nm in diameter.

Approximately 100 μL of the magnetic nanoparticle solution was added to the completed solution, leading to the modification and purification of the magnetic nanoparticles through electrostatic adsorption. The Au@DTNB@Ag nanoparticles were also modified using a similar procedure. The prepared SiMMs solution (2 mL) was centrifuged and washed three times with deionized water at 8 000 r/min for 10 min each. The precipitate was then mixed with 1.5 mL of deionized water and 100 μL of a 5% aqueous solution of glutaraldehyde, and placed on a shaker in a constant-temperature water bath overnight (8–12 h). Following this, the solution was centrifuged and washed three times with deionized water as before. Subsequently, 1.5 mL of deionized water was added, and the solution was shaken. 16 mg of AAPH was then added, and the tube was sealed, shielded from light, and left on a shaker in a constant-temperature water bath overnight (8–12 h) with ice packs to prevent AAPH decomposition. After completion of the reaction, the tube was removed, washed three times with deionized water.

Cell capture

100 μL of 5% glutaraldehyde aqueous solution was added to 1.5 mL of SiMMs-AAPH solution. After 12 h, the mixture was centrifuged 3 times with PBS solution, and then the lower precipitate was dissolved in 400 μL of PBS solution. After 1 μL of 1 mg/mL CD63 adapter was added, the centrifuge tube was placed on a constant temperature water bath shaker for 4 h and centrifuged to remove unbound adapters. After staining and being washed thrice with PBS, 400 μL of PBS was added. 100 μL of SiMMs-AAPH@CD63 micromotor solution was added to the stained eight-well plate, followed by being pipetted back and forth three times, sealed, and placed in a cell culture incubator for 2 h. We removed the eight-well plate, aspirated the supernatant, and washed it thrice with PBS to remove apoptotic cancer cells and SiMMs-AAPH micromotors that did not capture cells successfully. We placed the prepared samples under a Raman spectrometer for observation.

SERS mapping analysis

After completing cell capture, SERS mapping analysis was performed. Once data is collected, we processed the data and reconstructed images using the analysis tools provided by Labspec5.

Fluorescence imaging of SiMMs

Utilizing a fluorescence microscope, we initially

observe SiMMs drug-loaded micromotors under a bright-field using a 100× objective lens. Subsequently, FITC was excited using a 488-nm laser to observe the fluorescence characteristics of SiMMs, demonstrating their fluorescence tracking capability.

MSD motion analysis

Take 1 mL of the prepared SiMMs aqueous solution and place it in an 8-well plate. Use the ultra-high-resolution fluorescence microscope with ZEN software for capturing images. Brief steps are as follows: Locate the free SiMMs drug-loaded micromotors in the solution under the 100× oil lens field of view. Use a custom-made magnetic field to attract the SiMMs and control their directional movement. Set appropriate capture parameters in the ZEN software, with an exposure time of 100 ms, capturing 5 000 frames of images exported in video format. Import this video into image processing software ImageJ. Use the Particle Tracker plugin to extract particle motion trajectories. Export the trajectory data in text format and calculate the average mean square displacement (MSD) for each time interval using Excel. Plot the calculated MSD values against the time intervals, which the *x*-axis represents the time intervals, and the *y*-axis represents the corresponding MSD values. Use Origin software to draw the MSD curve.

Blood cell capture experiment

Initiate the procedure by performing membrane-specific fluorescent staining of MDA-MB-231 cells. Subsequently, add the stained MDA-MB-231 cells to normal human blood to simulate clinical tumor patient blood samples. Proceed with the cell capture experiment. Place the sample under a fluorescent microscope for co-localization imaging and observation. Use a magnetic field to control the motors and move them toward the vicinity of the cancer cells for targeted capture.

Detection of intracellular carbon-centered free radicals

Inoculate MDA-MB-231 cells in two wells of the same eight-well cell culture dish. After 48 h of incubation in the cell culture incubator, introduce SiMMs-AAPH@CD63 and non-drug-loaded SiMMs@CD63 into the respective wells and continue incubation in the incubator for 1.5 h. Following the incubation period, expose the eight-well plate to AMF for 1 h. Subsequently, wash the cells three times with PBS solution and stain them with 2 μmol/L H_2DCFDA probe at 37 °C for 30 min. Visualize with a fluorescence microscope using 488 nm laser excitation.

Cell viability staining

Take seven experimental groups, aspirate the culture medium, and add 150 μL of 2 μmol/L Calcein AM and 2 μL of propidium iodide (PI) to each sample. Return the 6 sets of samples to the cell culture incubator for 15 min to ensure thorough staining and prevent cell apoptosis due to external conditions. Afterward, remove the seven sets of samples, aspirate the supernatant, wash twice with PBS solution, add 400 μL of PBS buffer, and observe under a fluorescence microscope. Excite Calcein AM and PI using 488-nm and 543-nm lasers for imaging and observation.

Viability Assay

MDA-MB-231 cells were seeded in 96-well plates and incubated at 37 °C for 24 h. Subsequently, the cells were subjected to various treatments to assess their cytotoxic effects. After the incubation period, the CCK-8 solution was introduced and incubated for an additional 12 h. The percentage of viability was then adjusted based on the untreated cells.

Result and Discussion

Characterization of SiMMs

The fabrication process of SiMMs is shown in Fig. 1. The entire preparation process involves the preparation of silicon microtube carriers using a template method, as well as the functionalization treatment of carriers.

The morphology of SiMMs is analyzed using TEM, SEM and optical microscopy (Figs. 2(a)–2(c)). The TEM image of the prepared Fe_3O_4 magnetic nanoparticles shows their uniform size, approximately 50 nm, and excellent dispersibility. Images under bright-field optical microscopy unveil the uniform embedding of magnetic nanoparticles and core–shell gold-silver nanoparticles on the surface of SiMMs. In the SEM image of silica microtubes, the surface appears rough and exhibits a hollow columnar structure, with a length ranging approximately from 10 to 15 μm. The rough surface enhances the specific

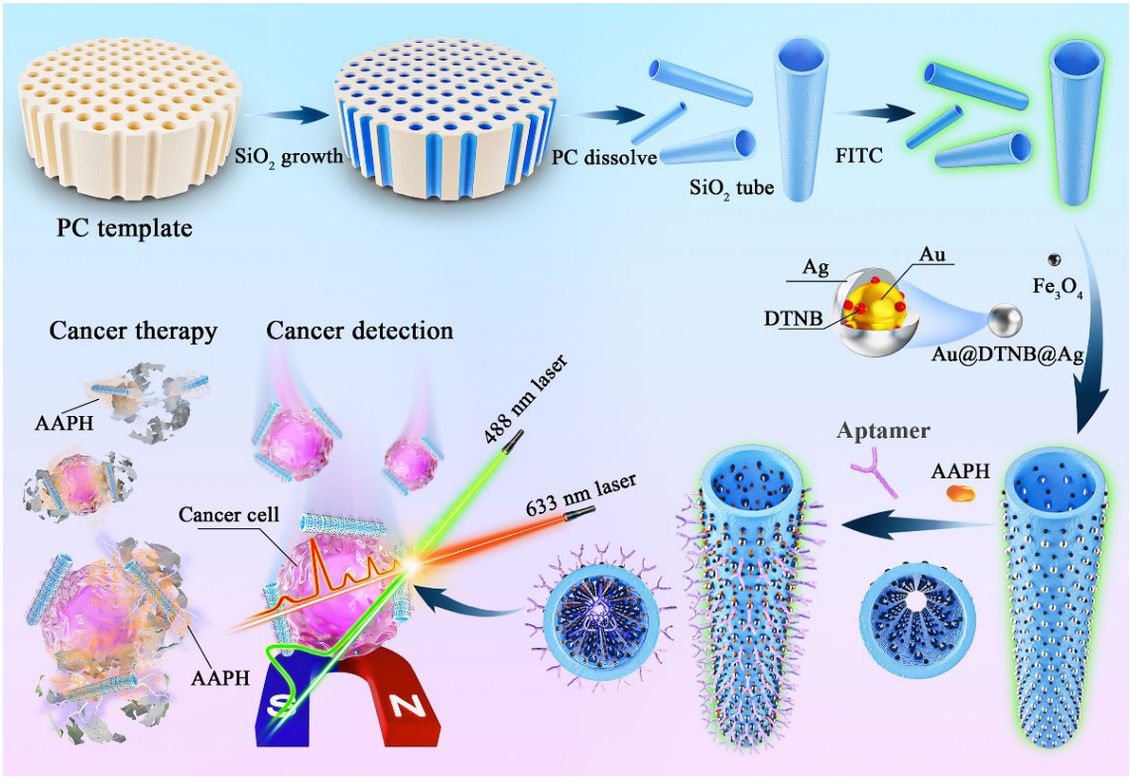

Fig. 1 Schematic diagram of the preparation process and working principle of SiMMs.

surface area, facilitating the entry of various functionalization factors into the interior of the microtubes, thereby maintaining the stability of drugs during transportation [41]. Additionally, the hollow structure facilitates fluid flow, which is advantageous for the movement of SiMMs in the bloodstream [42]. To validate the success of each step in the preparation of SiMMs, TEM, and energy-dispersive X-ray spectroscopy (EDX) elemental analysis is employed, as shown in Fig. 2(d). The red portion represents O elements, mainly derived from APTES and Fe_3O_4 nanoparticles. The yellow portion corresponds to Si elements from the silicon tubes. The blue portion represents Ag elements. The dark red portion stands for Au elements, both originating from the core–shell gold-silver nanoparticles. The green portion symbolizes Fe elements from the Fe_3O_4 magnetic nanoparticles. To further demonstrate the successful modification of SiMMs, the surface potential of SiMMs was characterized at different stages of the functionalization process, as shown in Fig. 2(e). The surface potential of the SiMMs framework is (18.76 ± 0.84) mV, positively charged. The negatively charged Fe_3O_4 magnetic nanoparticles and core–shell gold-silver SERS nanoprobes are easily modified into the positively charged SiMMs through strong electrostatic interactions, resulting in a surface potential of (–20.07 ± 2.57) mV for SiMMs. Subsequently, by linking the amino group on AAPH with the aldehyde group on the other end of glutaraldehyde to load AAPH onto the SiMMs, a partially neutral covering layer is formed that reduces the overall negative charge on the surface, leading to an increase in the surface potential of (–12.8 ± 0.40) mV for SiMMs loaded with AAPH (denoted as SiMMs-AAPH). Therefore, it can be demonstrated that SiMMs-AAPH were successfully prepared via a simple template-assisted ALD method.

Motion behaviors of SiMMs

The investigation into the motion trajectories of SiMMs under the influence of a magnetic field was conducted using optical microscopy, as shown in Fig. 3(a). The motion trajectories and mean square displacement (MSD) analysis results were consistent with those reported in the literature [43]. Due to the diameter of SiMMs being greater than 400 nm, the rotational diffusion coefficient of the micromotors was relatively low, resulting in stable motion under magnetic field control, in stark contrast to the random and uncoordinated motion of SiMMs observed in the absence of an AMF (Video S1 in the Electronic Supplementary Material (ESM)). All position data recorded in Fig. 3(a) was analyzed applying the MSD

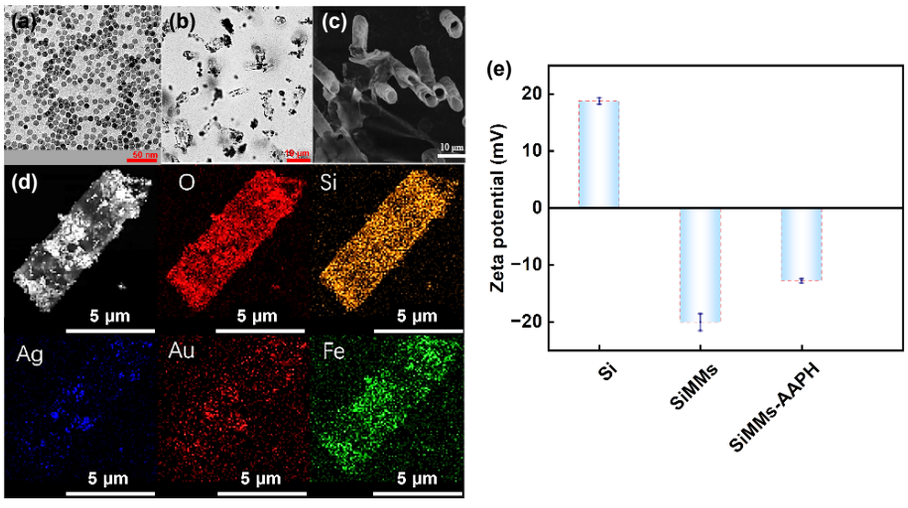

Fig. 2 Morphology and elemental characterization of SiMMs. **(a)** SEM image of Fe_3O_4 nanoparticles; **(b)** bright-field image of the complete structure; **(c)** SEM image of silica microtubes; **(d)** EDX elemental analysis of SiMMs; **(e)** surface zeta potential during the functionalization process of microtubes: (1) the potential of the prepared Si-based microtubes is (18.76 ± 0.84) mV; (2) the potential of the complete SiMMs is (–20.07 ± 2.57) mV; (3) the potential after drug loading is (–12.8 ± 0.40) mV.

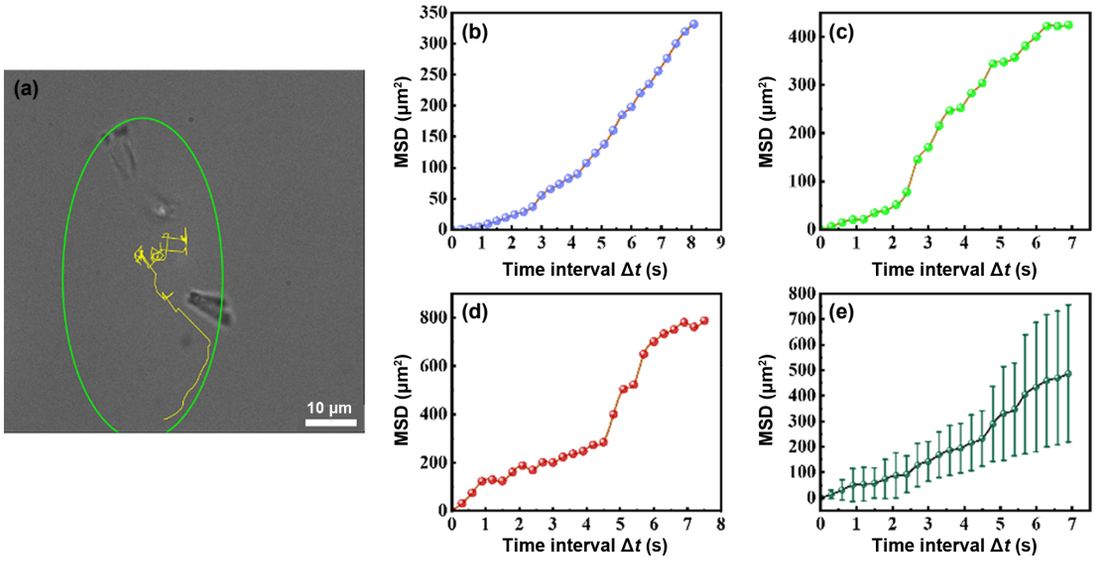

Fig. 3 (a) Motion tracking trajectories of SiMMs (44 s in Video S2 in the ESM); MSD of three individual SiMMs **(b)–(d)** and the averaged result **(e)**.

formula:

$$\mathrm{MSD} = |r(t) - r(0)|^2 \quad (1)$$

where r^2 represents the average of the squared displacements.

The analysis focused solely on the motion of individual particles, r^2 represents only the square of the displacement, $r(t)$ denotes a function of time, and $r(0)$ represents the original coordinates of the SiMMs. Figs. 3(b)–3(e) reveal an increasing slope of the MSD versus Δt over time, suggesting a consistent rate of drift in a particular direction. Analysis of the motion trajectories of three different SiMMs (Figs. 3(b)–3(d)) reveals no significant differences in MSD values. This demonstrates that the direction control of SiMMs during motion is precise, despite potential variations in speed. These results collectively confirmed the excellent magnetically controlled directional motion of SiMMs.

Optical tracking capability

The modification with FITC dye confers fluorescent properties to the SiMMs. Fig. 4(a) shows the fluorescence spectrum of SiMMs with an excitation wavelength of 488 nm, indicating an obvious FITC signal. Fig. 4(b) displays a bright-field image of the SiMMs under a fluorescence microscope, Fig. 4(c) shows the fluorescence image of the same SiMMs

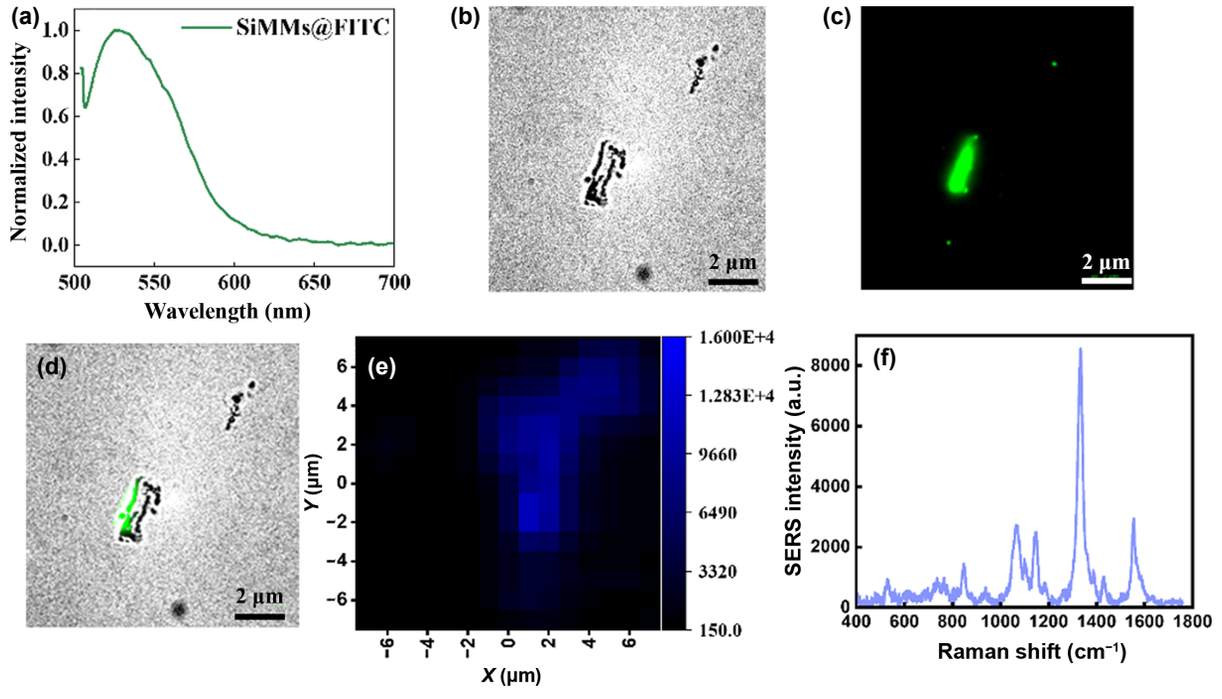

Fig. 4 (a) Fluorescence spectrum of SiMMs; **(b)** bright-field image of SiMMs under a fluorescence microscope; **(c)** fluorescence image of SiMMs under 488-nm excitation; **(d)** overlay of **(b)** and **(c)**; **(d)** SERS mapping of SiMMs incubated with MDA-MB-231 cells; **(e)** SERS spectrum of SiMMs.

under 488-nm laser excitation, with the entire microtube exhibiting green fluorescence. This characteristic provides strong support for subsequent cell capture using fluorescence co-localization techniques.

Despite numerous significant advantages of optical imaging techniques, fluorescence imaging still faces some challenges, such as the instability of continuous tracking with fluorescent dyes and their limited penetration ability when encountering deep tissues [44]. SERS tracking leverages the unique Raman signals on the surface of nanoparticles to identify SiMMs [45]. This technique offers unparalleled advantages in locating SiMMs in complex biological environments due to its extremely high sensitivity and specific molecular recognition capabilities [46]. Therefore, the combination of fluorescence imaging and SERS tracing is a fine choice.

To check the SERS tracking ability of the SiMMs working with cells, the MDA-MB-231 cells were captured using SiMMs (modified with CD63 aptamers), and SERS mapping was conducted on captured cells (Fig. 4(e)). Further analysis revealed that the SERS characteristic peaks of SiMMs were consistent with DTNB (Fig. 4(f)). The enhancement of SERS signal under cellular environment can be attributed to the higher surface roughness of SiMMs, facilitating the adsorption of more SERS probes, increasing the number of SERS hotspots, and significantly enhancing the SERS signal. The results demonstrated that SiMMs exhibit outstanding SERS tracking capabilities. The tracking in both SERS and fluorescence modes provides a powerful means for monitoring and tracking the treatment process. This combination offers a synergistic approach that maximizes the strengths of both techniques while addressing their respective limitations. Fluorescence tracking enables rapid and intuitive localization of SiMMs, while SERS signals validate and precisely pinpoint their positions, ensuring high detection accuracy. Furthermore, fluorescence allows real-time observation of SiMMs' dynamic changes, such as motion and distribution, whereas SERS can confirm critical events like drug release and cellular uptake. Together, these complementary techniques provide a comprehensive understanding of SiMMs' behavior in complex biological environments, significantly enhancing their potential for therapeutic applications.

Capture cancer cells in human blood

To validate the cell-capturing capability of SiMMs-AAPH drug-loaded micromotors in human blood, experiments were conducted to capture MDA-MB-231 cells using CD63 aptamer modified SiMMs-AAPH (denoted as SiMMs-AAPH@CD63). CD63, a

member of the lysosome-associated membrane protein family, is highly expressed on the surface of triple-negative breast cancer (MDA-MB-231) cells, making it an ideal target for this study. By employing the CD63 aptamer, which offers high affinity and specificity, we aimed to achieve effective recognition and capture of MDA-MB-231 cells, enhancing the targeting efficiency and therapeutic potential of the micromotors. Initially, cell capture experiments were performed in PBS buffer. Fluorescence microscopy was employed to observe the capturing status by co-localizing the fluorescence of SiMMs-AAPH and the stained cell membrane. Fig. 5(a) represents the channel excited by a 488-nm laser, displaying green fluorescence due to the FITC dye conjugated on SiMMs-AAPH. Fig. 5(b) corresponds to the channel excited by a 561-nm laser, showing red fluorescence from the DiD cell membrane dye with an emission wavelength of 663 nm. Fig. 5(c) depicts the overlay of the two images, indicating close proximity of the fluorescence signals from the FITC dye channel and the DiD-stained cell membrane channel, suggesting that SiMMs-AAPH are tightly connected to the cell surface. It was observed during the experiment that slight external disturbances did not cause detachment of SiMMs-AAPH from the cell surface, indicating the successful capture of MDA-MB-231 cells through SiMMs-AAPH@CD63.

To further validate the cancer cell capturing capability of SiMMs-AAPH@CD63 in human blood, we used blood samples from healthy individuals and added MDA-MB-231 cells to simulate the blood status of cancer patients. Cell capture experiments were conducted using this blood sample. Similarly, from the overlaid image (Fig. 5(f)), it is evident that SiMMs-AAPH@CD63 are present on the surface of MDA-MB-231 cells, indicating the successful capture of cancer cells in environment. Thus, the tumor cell-targeting capture ability of SiMMs is unaffected by the complex blood environment.

Generation of intracellular free radicals

AAPH generates a substantial amount of carbon-centered radicals under heated conditions. To verify that SiMMs-AAPH@CD63 can produce localized heating and decompose the AAPH loaded onto SiMMs-AAPH@CD63 under AMF, we investigated the generation of free radicals using the H_2DCFDA probe. H_2DCFDA is a non-fluorescent compound that penetrates live cells and is oxidized by radicals to produce the highly fluorescent 2',7'-dichlorofluorescein (DCF). The excitation

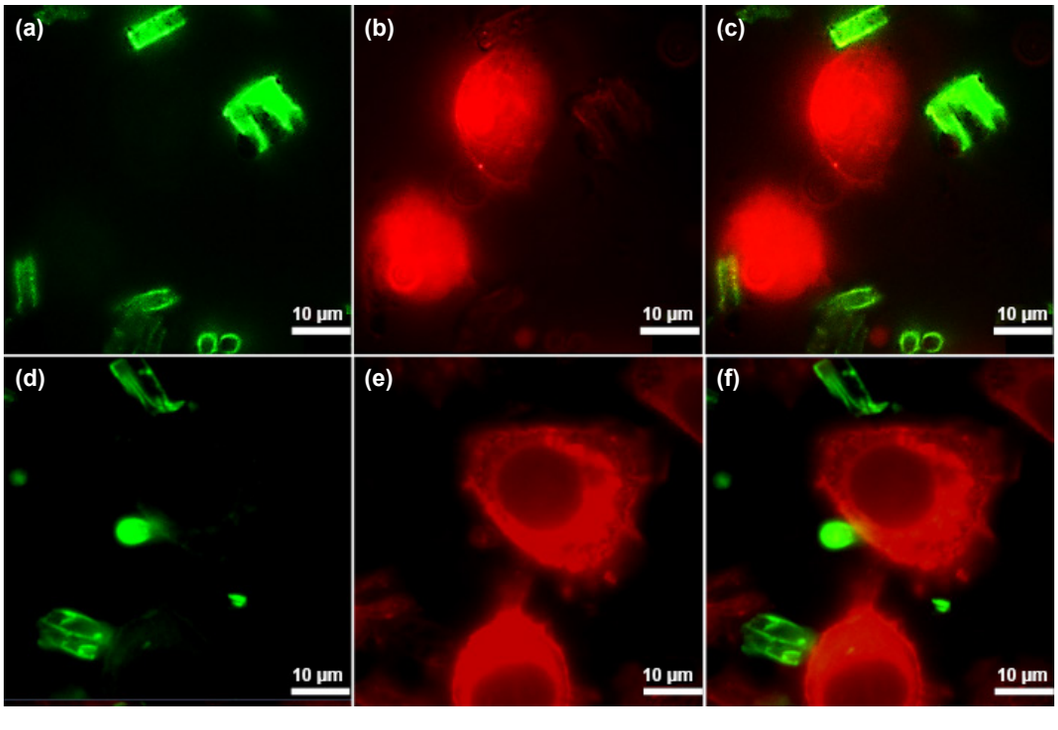

Fig. 5 Capture of MDA-MB-231 cells by SiMMs-AAPH@CD63. In PBS: **(a)** FITC dye channel; **(b)** DiD stained cell membrane channel; **(c)** overlay of channels **(a)** and **(b)**; in blood: **(d)** FITC dye channel; **(e)** DiD stained cell membrane channel; **(f)** overlay of channels **(d)** and **(e)**.

wavelength for DCF is 492–495 nm, and the emission wavelength is 517–527 nm [47]. Four control groups were set up to eliminate other factors that could interfere with the experiment. Fig. 6(a) represents untreated cells. Fig. 6(b) represents the second control group where only AAPH was added to the well plate. Fig. 6(c) displays the third control group, where SiMMs-AAPH without CD63 were added to the well plate. In the fourth control group depicted in Fig. 6(d), SiMMs@CD63 without AAPH were added, and the well plate was placed under AMF for 30 min. It is evident from the images that in the four control groups, only low background green fluorescence signals were observed, the results showed that untreated cells exhibited a low level of green fluorescence. This indicates that while carbon-centered radicals are naturally produced during cellular metabolic processes, their levels are relatively low under normal physiological conditions. However, in Fig. 6(e), under AMF, MDA-MB-231 cells treated with SiMMs-AAPH@CD63 exhibit bright green fluorescence signals. This observation suggests that the prepared drug-loaded micromotors can indeed generate a high level of free radicals within the cells under AMF.

Therapy effects *in vitro*

Having confirmed the ability of SiMMs-AAPH@CD63 to generate free radicals in MDA-MB-231 cells, we further investigated the *in vitro* anticancer potential of SiMMs-AAPH@CD63. To elucidate the synergistic anticancer effects of SiMMs-AAPH@CD63, confocal laser scanning microscopy (CLSM) was employed to directly observe live and dead cells based on fluorescence signals. Live cells were stained with Calcein AM, while dead cells were stained with PI. As shown in Figs. 7(a)–7(e), significant green fluorescence signals were observed in the AAPH treatment group, SiMMs treatment group, SiMMs-AAPH treatment group, and AAPH+AMF treatment group, with sporadic red fluorescence attributed to natural apoptosis of MDA-MB-231 cells. This indicates that SiMMs-AAPH and AMF individually demonstrate high biocompatibility and low cytotoxicity. In contrast, when MDA-MB-231 cells were incubated with SiMMs under AMF for 30 min, the CLSM images displayed an increase in red fluorescence signals (Fig. 7(f)). This result validates that the magnetic hyperthermia effect of SiMMs can induce cell death in MDA-MB-231 cancer cells to a certain extent, although the lethality is limited. Importantly, when MDA-MB-231 cells were incubated with SiMMs-AAPH and then subjected to AMF, a significant increase in red fluorescence signals was observed (Fig. 7(g)). These findings confirmed that the combination of free radicals generated by SiMMs-AAPH and magnetic hyperthermia under AMF can effectively kill MDA-MB-231 cancer cells, enhancing the efficacy of magnetic hyperthermia.

Furthermore, the *in vitro* therapeutic potential of SiMMs-AAPH@CD63 was investigated via cell counting CCK-8 assay. As shown in Fig. 7(h), no significant cytotoxicity was detected after incubating MDA-MB-231 cells with AAPH, SiMMs, SiMMs-AAPH, and AAPH+AMF for 12 h. We then assessed the AMF-stimulated cytotoxicity of SiMMs toward MDA-MB-231 cells. The survival rate of MDA-MB-231 cells treated with SiMMs+AMF declined to 72.7% upon AMF stimulation for 30 min. Importantly, SiMMs-AAPH exhibited augmented anticancer efficacy in comparison with that of SiMMs under AMF. The cellular survival rate was approximately 32.8% for the SiMMs-AAPH+AMF group, which was markedly less than that of 72.7% for the SiMMs+AMF group under the same condition. These results indicated that the rapid generation of free radicals induced by the magnetic

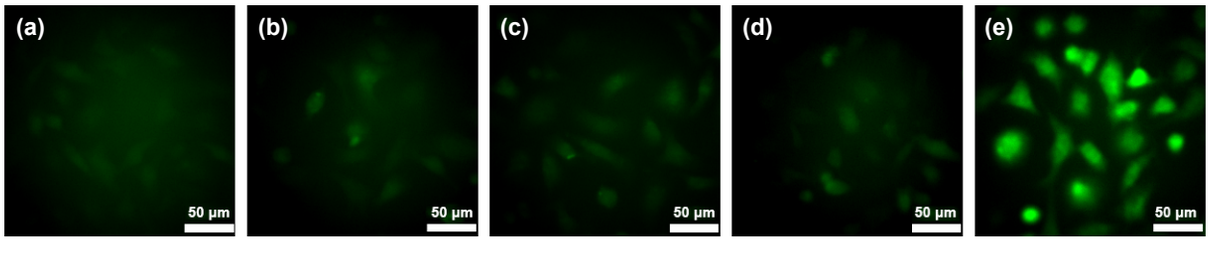

Fig. 6 Experiment on the generation of intracellular carbon-centered free radicals. **(a)** Untreated cells; **(b)** cells treated with only AAPH; **(c)** cells treated with SiMMs-AAPH; **(d)** cells treated with SiMMs@CD63 and subjected to AMF; **(e)** cells treated with SiMMs-AAPH@CD63 and subjected to AMF.

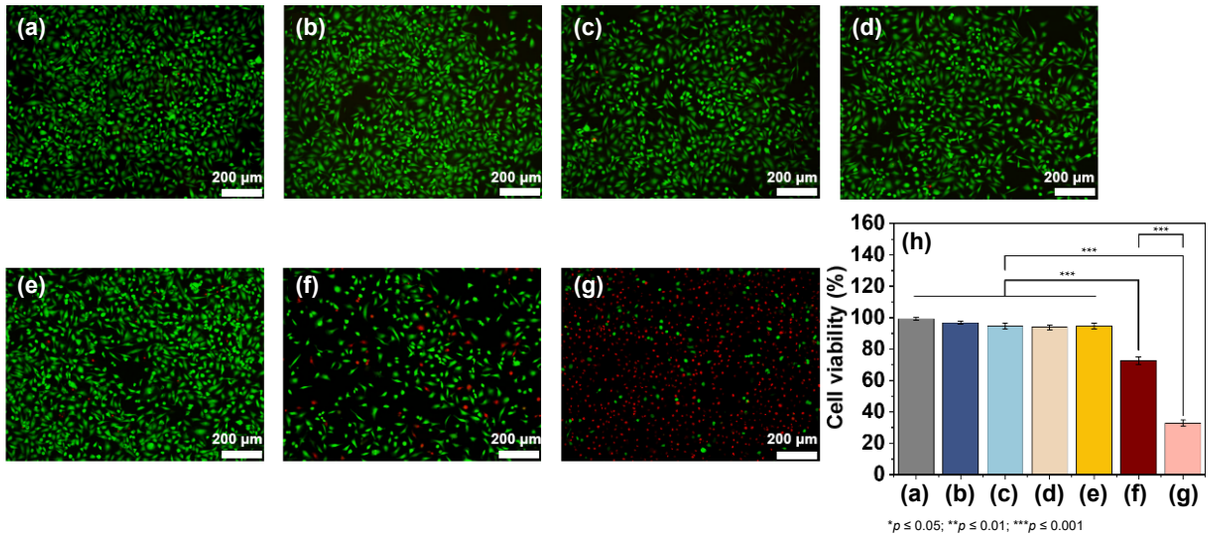

Fig. 7 Fluorescent images of MDA-MB-231 cells stained for live-dead viability assay. **(a)** Cells treated with PBS; **(b)** cells treated with AAPH; **(c)** cells treated with SiMMs@CD63; **(d)** cells treated with SiMMs-AAPH@CD63; **(e)** cells treated with AAPH and subjected to AMF; **(f)** cells treated with SiMMs@CD63 and subjected to AMF; **(g)** cells treated with SiMMs-AAPH@CD63 and subjected to AMF; **(h)** CCK-8 assay of the viability of MDA-MB-231 cells under different treatments. To be considered statistically significant, the *P* value should be < 0.05. The range of *P* values is indicated by the number of the label *, i.e., $*P < 0.05$; $**P < 0.01$; $***P < 0.001$.

hyperthermia effect can effectively accelerate cancer cell death, further validating the synergistic therapeutic effect of magnetic hyperthermia and free radicals.

To assess the efficacy and advantages of SiMMs, we conducted a survey of existing drug delivery micromotors (Table 1). As shown in Table 1, other drug-loaded micromotors typically rely on a single tracking method, such as fluorescence, MR or IR, though widely used, have inherent drawbacks. For instance, MRI-based systems, such as Fe_3O_4@PTADE and PHIONs-AIPH, can suffer from limited spatial resolution, especially when targeting small or deep tissue regions. Furthermore, MRI is typically more expensive and requires specialized equipment. Similarly, IR imaging, used in IONC-AAPH, has lower sensitivity compared to fluorescence or SERS, particularly in detecting low concentrations of micromotors. It can also be hindered by tissue scattering, limiting its effectiveness *in vivo*. In contrast, SiMMs leverage both SERS and fluorescence for real-time tracking, combining the high sensitivity and specificity of fluorescence with the unique Raman fingerprinting capability of SERS. This dual-mode approach not only provides better sensitivity and precision in tracking but also overcomes the limitations of single imaging techniques, enhancing both therapeutic monitoring and treatment efficacy.

Additionally, SiMMs achieve a killing efficiency of 72.7%, which is competitive when compared to other micromotors. The combination of these features positions SiMMs as a promising candidate for targeted drug delivery and therapeutic applications, offering advantages in real-time monitoring and therapeutic precision over existing systems.

Table 1 Comparison of different types of drug-loaded micromotors.

Type of drug-loaded micromotor	Tracking method	Killing efficiency
IONC-AAPH [11]	IR	52.1%
MSN-Pt@TA [48]	Fluorescence	85.2%
Fe_3O_4@PTADE [47]	MRI	49.6%
PHIONs-AIPH [49]	MRI	70%
Mag@MSNs@AIPH[50]	MRI	80%
PHPF NMs [51]	Fluorescence	78%
SiMMs-AAPH (this work)	SERS and fluorescence	72.7%

Conclusions

SiMMs is promising for drug delivery and targeted cancer therapy. To enhance SiMMs' therapeutic potential, a multifunctional magnetic hyperthermia-responsive drug-loaded micromotor was fabricated by integrating silicon microtubes, magnetic nanoparticles, metal nanoparticles, and biological ligands. This functionalized micromotor combined magnetic guidance, drug delivery, and real-time monitoring modules, realizing magnetic hyperthermia-free radical synergistic therapy. Such a controlled and targeted strategy could enhance the efficiency of chemotherapy while concurrently reducing side effects toward healthy tissues, which holds excellent prospects in anticancer therapy. Such a controlled and targeted strategy could enhance the efficiency of chemotherapy while concurrently reducing side effects toward healthy tissues, which holds excellent prospects in anticancer therapy. Future efforts will focus on improving biodegradability, biocompatibility, and targeting efficiency to advance the *in vivo* and clinical applications of SiMMs.

CRediT Author Statement

Sijie Zhang: writing original draft, visualization, validation, investigation, and data curation. **Gaoqiang Yin:** methodology, software, and conceptualization. **Zuyao Wang:** methodology. **Lei Wu:** funding acquisition. **Kuo Yang:** funding acquisition. **Ruohu Zhang:** funding acquisition. **Shenfei Zong:** writing–review, editing, project administration, methodology, investigation, funding acquisition, formal analysis, and conceptualization. **Zhuyuan Wang:** project administration and funding acquisition. **Yiping Cui:** supervision, resources, project administration, and funding acquisition.

Acknowledgements

This work was supported by the Natural Science Foundation of China (NSFC) (Nos. 62175027, 62175030, 62305054, and 62205053).

Conflict of Interests

The authors declare that they have no known competing financial interests or personal relationships that could have appeared to influence the work reported in this paper.

Supporting Information

Supporting information to this article can be found online at https://doi.org/10.26599/NBE.2025.9290118.

References

[1] J.L. Markman, A. Rekechenetskiy, E. Holler, et al. Nanomedicine therapeutic approaches to overcome cancer drug resistance. *Advanced Drug Delivery Reviews*, 2013, 65(13-14): 1866−1879. https://doi.org/10.1016/j.addr.2013.09.019

[2] M.P.V. Shekhar. Drug resistance: Challenges to effective therapy. *Current Cancer Drug Targets*, 2011, 11(5): 613−623. https://doi.org/10.2174/156800911795655921

[3] N. Iyengar. The emperor of all maladies. *Australian Journal of General Practice*, 2023, 52(5): 327. https://doi.org/10.31128/ajgp-12-22-6651

[4] I. Fraunholz, K. Grau, C. Weiss, et al. Patient- and treatment-related risk factors for nausea and emesis during concurrent chemoradiotherapy. *Strahlentherapie und Onkologie*, 2011, 187(1): 1−6. https://doi.org/10.1007/s00066-010-2196-0

[5] P.J. Hesketh, M. Aapro, J.C. Street, et al. Evaluation of risk factors predictive of nausea and vomiting with current standard-of-care antiemetic treatment: Analysis of two phase III trials of aprepitant in patients receiving cisplatin-based chemotherapy. *Supportive Care in Cancer*, 2010, 18(9): 1171−1177. https://doi.org/10.1007/s00520-009-0737-9

[6] C. Pirri, P. Katris, J. Trotter, et al. Risk factors at pretreatment predicting treatment-induced nausea and vomiting in Australian cancer patients: A prospective, longitudinal, observational study. *Supportive Care in Cancer*, 2011, 19(10): 1549−1563. https://doi.org/10.1007/s00520-010-0982-y

[7] W.B. Jiao, L.J. Dai, B. Yan, et al. Heating up the immune battle: Magnetic hyperthermia against cancer. *Fundamental Research*, 2024. https://doi.org/10.1016/j.fmre.2024.08.006

[8] E. Cazares-Cortes, S. Cabana, C. Boitard, et al. Recent insights in magnetic hyperthermia: From the "hot-spot" effect for local delivery to combined magneto-photo-thermia using magneto-plasmonic hybrids. *Advanced Drug Delivery Reviews*, 2019, 138: 233−246. https://doi.org/10.1016/j.addr.2018.10.016

[9] Y. Chao, G.B. Chen, C. Liang, et al. Iron nanoparticles for low-power local magnetic hyperthermia in combination with immune checkpoint blockade for systemic antitumor therapy. *Nano Letters*, 2019, 19(7): 4287−4296. https://doi.org/10.1021/acs.nanolett.9b00579

[10] J. Pan, Y.Y. Xu, Q.S. Wu, et al. Mild magnetic hyperthermia-activated innate immunity for liver cancer therapy. *Journal of the American Chemical Society*, 2021, 143(21): 8116−8128. https://doi.org/10.1021/jacs.1c02537

[11] L.L. Zhang, Q.B. Zhang, D.T. Hinojosa, et al. Multifunctional magnetic nanoclusters can induce immunogenic cell death and suppress tumor recurrence and metastasis. *ACS Nano*, 2022, 16(11): 18538−18554. https://doi.org/10.1021/acsnano.2c06776

[12] I.H. Ifijen, A.T. Christopher, O.K. Lekan, et al.

Advancements in tantalum based nanoparticles for integrated imaging and photothermal therapy in cancer management. *RSC Advances*, 2024, 14(46): 33681−33740. https://doi.org/10.1039/D4RA05732E

[13] H. Gavilán, S.K. Avugadda, T. Fernández-Cabada, et al. Magnetic nanoparticles and clusters for magnetic hyperthermia: Optimizing their heat performance and developing combinatorial therapies to tackle cancer. *Chemical Society Reviews*, 2021, 50(20): 11614−11667. https://doi.org/10.1039/D1CS00427A

[14] T.J. Carter, G. Agliardi, F.Y. Lin, et al. Potential of magnetic hyperthermia to stimulate localized immune activation. *Small*, 2021, 17(14): e2005241. https://doi.org/10.1002/smll.202005241

[15] G.M. Huang, Y. Qiu, F.F. Yang, et al. Magnetothermally triggered free-radical generation for deep-seated tumor treatment. *Nano Letters*, 2021, 21(7): 2926−2931. https://doi.org/10.1021/acs.nanolett.1c00009

[16] X.D. Zuo, D.M. Zhang, J.D. Zhang, et al. Oxygen vacancy enhanced magnetic heating efficiency of ferrite nanoparticles for self-regulating temperature hyperthermia. *Ceramics International*, 2023, 49(22): 36885−36893. https://doi.org/10.1016/j.ceramint.2023.09.019

[17] R. Das, N.P. Kim, S.B. Attanayake, et al. Role of magnetic anisotropy on the hyperthermia efficiency in spherical $Fe_{3-x}Co_xO_4$ (x = 0–1) nanoparticles. *Applied Sciences*, 2021, 11(3): 930. https://doi.org/10.3390/app11030930

[18] A. Hajalilou, L.P. Ferreira, M.E. Melo Jorge, et al. Surface-modified iron oxide nanoparticles with natural biopolymers for magnetic hyperthermia: Effect of reducing agents and type of biopolymers. *Journal of Composites Science*, 2024, 8(10): 425. https://doi.org/10.3390/jcs8100425

[19] P. Kovacic, R.S. Pozos, R. Somanathan, et al. Mechanism of mitochondrial uncouplers, inhibitors, and toxins: Focus on electron transfer, free radicals, and structure-activity relationships. *Current Medicinal Chemistry*, 2005, 12(22): 2601−2623. https://doi.org/10.2174/092986705774370646

[20] M. Valko, M. Izakovic, M. Mazur, et al. Role of oxygen radicals in DNA damage and cancer incidence. *Molecular and Cellular Biochemistry*, 2004, 266(1-2): 37−56. https://doi.org/10.1023/B:MCBI.0000049134.69131.89

[21] M. Valko, C.J. Rhodes, J. Moncol, et al. Free radicals, metals and antioxidants in oxidative stress-induced cancer. *Chemico-Biological Interactions*, 2006, 160(1): 1−40. https://doi.org/10.1016/j.cbi.2005.12.009

[22] L.L. Feng, S.L. Gai, Y.L. Dai, et al. Controllable generation of free radicals from multifunctional heat-responsive nanoplatform for targeted cancer therapy. *Chemistry of Materials*, 2018, 30(2): 526−539. https://doi.org/10.1021/acs.chemmater.7b04841

[23] D. García-Soriano, P. Milán-Rois, N. Lafuente-Gómez, et al. Multicore iron oxide nanoparticles for magnetic hyperthermia and combination therapy against cancer cells. *Journal of Colloid and Interface Science*, 2024, 670: 73−85. https://doi.org/10.1016/j.jcis.2024.05.046

[24] Y. Chen, X. Zhang, L. Wu, et al. Lipid nanoparticles for the controlled generation of free radicals and effective treatment of hypoxic cancer. *Chemistry Letters*, 2020, 49(7): 817−819. https://doi.org/10.1246/cl.200228

[25] N. Gupta, C. Gupta, S. Sharma, et al. Magnetic iron oxide nanoparticles encapsulating horseradish peroxidase (HRP): Synthesis, characterization and carrier for the generation of free radicals for potential applications in cancer therapy. *RSC Advances*, 2016, 6(112): 111099−111108. https://doi.org/10.1039/C6RA24586B

[26] L. Ruan, K. Zhao, X.R. Tian, et al. Macrophages exosomes-coated Fe_3O_4 nanoparticles for oxygen independent generation of free radicals and hypoxic cancer therapy. *Materials Today Communications*, 2022, 33: 104672. https://doi.org/10.1016/j.mtcomm.2022.104672

[27] H. Aslam, S. Shukrullah, M.Y. Naz, et al. Current and future perspectives of multifunctional magnetic nanoparticles based controlled drug delivery systems. *Journal of Drug Delivery Science and Technology*, 2022, 67: 102946. https://doi.org/10.1016/j.jddst.2021.102946

[28] T. Zhou, K. Zhu, Z.Y. Yang, et al. Chemically powered nanomotors with magnetically responsive function for targeted delivery of exosomes. *Small*, 2024, 20(37): e2311207. https://doi.org/10.1002/smll.202311207

[29] M.Y. Gai, J. Frueh, N. Hu, et al. Self-propelled two dimensional polymer multilayer plate micromotors. *Physical Chemistry Chemical Physics*, 2016, 18(5): 3397−3401. https://doi.org/10.1039/C5CP07697H

[30] S. Fusco, H.W. Huang, K.E. Peyer, et al. Shape-switching microrobots for medical applications: The influence of shape in drug delivery and locomotion. *ACS Applied Materials & Interfaces*, 2015, 7(12): 6803−6811. https://doi.org/10.1021/acsami.5b00181

[31] B.R. Xu, B.R. Zhang, L. Wang, et al. Tubular micro/nanomachines: From the basics to recent advances. *Advanced Functional Materials*, 2018, 28(25): 1705872. https://doi.org/10.1002/adfm.201705872

[32] Z.G. Wu, X.K. Lin, Y.J. Wu, et al. Near-infrared light-triggered "on/off" motion of polymer multilayer rockets. *ACS Nano*, 2014, 8(6): 6097−6105. https://doi.org/10.1021/nn501407r

[33] L.K.E. A. Abdelmohsen, M. Nijemeisland, G.M. Pawar, et al. Dynamic loading and unloading of proteins in polymeric stomatocytes: Formation of an enzyme-loaded supramolecular nanomotor. *ACS Nano*, 2016, 10(2): 2652−2660. https://doi.org/10.1021/acsnano.5b07689

[34] Q. Wang, Y. Wang, B.Y. Guo, et al. Novel heparin-loaded mesoporous tubular micromotors formed *via* template-assisted electrochemical deposition. *Journal of Materials Chemistry B*, 2019, 7(16): 2688−2695. https://doi.org/10.1039/C9TB00131J

[35] I.I. Slowing, J.L. Vivero-Escoto, C.W. Wu, et al. Mesoporous silica nanoparticles as controlled release drug delivery and gene transfection carriers. *Advanced Drug Delivery Reviews*, 2008, 60(11): 1278−1288. https://doi.org/10.1016/j.addr.2008.03.012

[36] X. Ma, A.C. Hortelao, A. Miguel-López, et al. Bubble-free propulsion of ultrasmall tubular nanojets powered by biocatalytic reactions. *Journal of the American Chemical Society*, 2016, 138(42): 13782−13785. https://doi.org/10.1021/jacs.6b06857

[37] C. Zhang, L.Y. Zhang, Y.Y. Ma, et al. Design of ultrasmall silica nanoparticles for versatile biomedical application in oncology: A review. *Nano Biomedicine and Engineering*, 2023, 15(4): 436−450. https://doi.org/10.26599/nbe.2023.9290044

[38] N.P. Dasgupta, H.B.R. Lee, S.F. Bent, et al. Recent advances in atomic layer deposition. *Chemistry of Materials*, 2016, 28(7): 1943−1947. https://doi.org/10.1021/acs.chemmater.6b00673

[39] T. Kumeria. Advances on porous nanomaterials for biomedical application (drug delivery, sensing, and tissue engineering). *ACS Biomaterials Science & Engineering*, 2022, 8(10): 4025−4027. https://doi.org/10.1021/acsbiomaterials.2c01103

[40] D.C. Zhao, N.L. Yang, L.K. Xu, et al. Hollow structures as drug carriers: Recognition, response, and release. *Nano Research*, 2022, 15(2): 739−757. https://doi.org/10.1007/s12274-021-3595-5

[41] A. Kusumi, Y. Sako, M. Yamamoto. Confined lateral

diffusion of membrane receptors as studied by single particle tracking (nanovid microscopy). Effects of calcium-induced differentiation in cultured epithelial cells. *Biophysical Journal*, 1993, 65(5): 2021−2040. https://doi.org/10.1016/S0006-3495(93)81253-0

[42] R.E. Darienzo, J.M. Wang, O. Chen, et al. Surface-enhanced Raman spectroscopy characterization of breast cell phenotypes: Effect of nanoparticle geometry. *ACS Applied Nano Materials*, 2019, 2(11): 6960−6970. https://doi.org/10.1021/acsanm.9b01436

[43] O. Karaman, G.A. Alkan, C. Kizilenis, et al. Xanthene dyes for cancer imaging and treatment: A material odyssey. *Coordination Chemistry Reviews*, 2023, 475: 214841. https://doi.org/10.1016/j.ccr.2022.214841

[44] K.J. Freedman, C.R. Crick, P. Albella, et al. On-demand surface- and tip-enhanced Raman spectroscopy using dielectrophoretic trapping and nanopore sensing. *ACS Photonics*, 2016, 3(6): 1036−1044. https://doi.org/10.1021/acsphotonics.6b00119

[45] V.T. Hoang, L.T. Tufa, J. Lee, et al. Tunable SERS activity of $Ag@Fe_3O_4$ core-shell nanoparticles: Effect of shell thickness on the sensing performance. *Journal of Alloys and Compounds*, 2023, 933: 167649. https://doi.org/10.1016/j.jallcom.2022.167649

[46] L.J. Jia, Z.Y. Li, D.D. Zheng, et al. A targeted and redox/pH-responsive chitosan oligosaccharide derivatives based nanohybrids for overcoming multidrug resistance of breast cancer cells. *Carbohydrate Polymers*, 2021, 251: 117008. https://doi.org/10.1016/j.carbpol.2020.117008

[47] A. Morales, C. Garcia-Ruiz, J.C. Fernandez-Checa. Reply to: "2', 7'-Dichlorofluorescein is not a probe for the detection of reactive oxygen and nitrogen species". *Journal of Hepatology*, 2012, 56(5): 1216−1217. https://doi.org/10.1016/j.jhep.2011.11.005

[48] X.X. Wang, H.R. Ma, Y.X. Guo, et al. Mesoporous Organosilica-Platinum Janus nanomotor coordinated by charge reversal for deep tumor penetration and promoted chemotherapy. *Chemical Engineering Journal*, 2024, 490: 151777. https://doi.org/10.1016/j.cej.2024.151777

[49] Q.L. Xiao, P.Y. Chen, M.R. Chen, et al. Correction: Design of an imaging magnetic microsphere based on photopolymerization for magnetic hyperthermia in tumor therapy. *Drug Delivery and Translational Research*, 2024, 14(3): 839. https://doi.org/10.1007/s13346-023-01434-4

[50] Y.J. Shen, C.H. Dong, H.J. Xiang, et al. Engineering oxygen-irrelevant radical nanogenerator for hypoxia-independent magnetothermodynamic tumor nanotherapy. *Small Methods*, 2021, 5(4): 2001087. https://doi.org/10.1002/smtd.202001087

[51] Y.W. Zhang, K. Zhang, H.N. Yang, et al. Highly penetrable drug-loaded nanomotors for photothermal-enhanced ferroptosis treatment of tumor. *ACS Applied Materials & Interfaces*, 2023, 15(11): 14099−14110. https://doi.org/10.1021/acsami.3c00297